(Preprint) AAS 25-331

PASSIVELY-SAFE OPTIMAL CISLUNAR RELATIVE MOTION USING LOCAL TOROIDAL COORDINATES

Yuji Takubo*, Walter J. Manuel†, and Simone D'Amico‡

Relative orbit design in the restricted three-body problem is gaining prominence with renewed interest in cislunar exploration. This paper develops bounded relative motion control strategies in the Circular Restricted Three-Body Problem (CR3BP) with passive safety, which maintains a miss distance even in the event of a sudden loss of control authority. This is done by leveraging the Local Toroidal Coordinates (LTC), which are built upon the local eigenspace of a quasi-periodic orbit. Using the LTC, a geometric analogy between quasi-periodic relative motion in the CR3BP and periodic relative motion in the restricted two-body problem is articulated. In addition, relative dynamics are newly derived in a co-moving velocity-based frame, extending beyond the traditional local-vertical-local-horizontal frame. Two fault-tolerant reconfiguration strategies between quasi-periodic relative orbits are presented as nonconvex optimal control problems in this frame, solved via sequential convex programming. A novel geometric constraint in the local toroidal coordinates offers an intuitive passive safety criterion, enabling safe relative motion control. By extending and generalizing well-known concepts from the two- to the three-body problem, this paper lays the foundation for the practical cislunar relative motion control schemes.

INTRODUCTION

Distributed Space Systems (DSS) are becoming more commonplace, particularly in applications involving spacecraft constellations, swarms, formations, and Rendezvous, Proximity Operations, and Docking (RPOD). The projected launch and deployment of NASA's Gateway in a Near-Rectilinear Halo Orbit (NRHO) will motivate RPOD operations of both crewed and uncrewed spacecraft to support lunar exploration and space logistics. DSS operating in the cislunar domain require Guidance, Navigation, and Control (GNC) algorithms that enable bounded relative motion between multiple spacecraft in the encountered multi-body dynamics.

Traditionally, dynamics models and state representations for relative motion between spacecraft rely on a fundamental assumption of orbiting around a single primary (e.g., Earth) based on the restricted two-body problem with additional perturbations. For example, the Hill-Clohessy-Wiltshire (HCW)[1] and the Yamanaka-Ankersen (YA) state transition matrices (STM)[2] focus on a near-circular and elliptic orbit, respectively, which are derived in the Local-Vertical-Local-Horizontal (LVLH) frame, also known as the Radial-Tangential-Normal (RTN) frame. In the last few decades, dynamics using a state representation in Relative Orbital Elements (ROE)[3] has also been developed, including various perturbations such as geopotential spherical harmonics to various degrees, solar radiation pressure, atmospheric drag, and third-body perturbations.[4,5] These linear relative dynamics models have a rich flight heritage in missions such as PRISMA,[6] TanDEM-X,[7] Starling,[8] SWARM-EX,[9] and VISORS.[10] Early research on relative motion with respect to a (virtual) spacecraft on the periodic orbit in the Restricted Three-Body Problem (R3BP) begins with the linearization of the nonlinear dynamics in the rotating frame,[7,11,12] which naturally aligns with the formulation of the R3BPs. More recently, relative dynamics of the Circular Restricted Three-Body Problem (CR3BP) and the Elliptic Restricted Three-Body Problem (ER3BP) have been derived in the LVLH frame.[13,14] This is further

*PhD Student, Department of Aeronautics and Astronautics, Stanford University, Stanford, CA 94305.
†PhD Candidate, Department of Aeronautics and Astronautics, Stanford University, Stanford, CA 94305.
‡Associate Professor, Department of Aeronautics and Astronautics, Stanford University, Stanford, CA 94305.

extended to the Bi-Circular Restricted Four-Body Problem (BCR4BP) to express a higher-fidelity dynamics model in the Sun-Earth-Moon system.[15]

There are two main streams of research for constructing a bounded relative motion with respect to a spacecraft in the R3BP. The first approach is to define a geometric relationship in relative motion from the equations of motion.[12] Some research introduces augmented dynamics by designing a corresponding continuous-time control law[11,16,17] to realize a specific geometry of forced relative orbits. The second approach leverages a fundamental solution space in the autonomous dynamics of the CR3BP in the Earth-Moon rotating frame. The CR3BP contains fundamental equilibrium solutions such as five libration points and periodic orbit families surrounding them. Furthermore, Quasi-Periodic Orbits (QPO) exist that naturally trace the surface of a Quasi-Periodic Invariant Torus (QPIT) and envelope the nearby energy-matching periodic orbit without an intersection.[18] Thus, a spacecraft on a QPO performs not only a quasi-periodic bounded motion with respect to the attractor (e.g., Moon) in the rotating frame but also a quasi-periodic bounded relative motion with respect to a spacecraft in its co-moving orbital frame. For this reason, applications of QPOs to long-term formation-flight and proximity operation missions have been widely investigated.[14,18,19] State-of-the-art demonstrations of the QPO-based relative motion control include a Linear Quadratic Regulator (LQR) controller and the Extended Kalman Filter for the formation reconfiguration in the BCR4BP[20] and chance-constrained model predictive control.[21] In this paper, such a QPO and the corresponding QPIT that is resolved in the local frame are denoted as Quasi-Periodic Relative Orbit (QPRO) and Quasi-Periodic Relative Invariant Tori (QPRIT) to make a clear distinction. Although QPO (QPIT) and QPRO (QPRIT) are the same trajectories (toroidal surfaces) that are resolved in the different coordinate frames, the former revolves around the attractor (or a libration point), while the latter revolves around a spacecraft on the periodic orbit in the CR3BP. Recently, a new state representation for the relative motion with respect to a spacecraft on a CR3BP's periodic orbit, known as Local Toroidal Coordinates (LTC), has been derived from the local eigenspace of a periodic orbit.[19,22] The coordinates defined in this frame are fundamentally related to the geometric configuration of a QPRO, which offers a convenient first-order condition of the bounded relative motion between spacecraft in (quasi-)periodic orbits in the CR3BP.

Although extensive research on the bounded relative motion in the cislunar domain has been performed, little attention has been paid to rigorous safety criteria. Specifically, this paper addresses the guarantee of sufficient separation between spacecraft even for free-drift trajectories that emanate from a sudden loss of control authority, also called passive safety.[23–26] Traditionally, the relative dynamics derived in the LVLH frame or Radial-Tangential-Normal (RTN) frame offer a convenient state representation of relative motion between spacecraft in the CR3BP. However, one critical limitation is that the tangential axis does not align with the chief's velocity direction, particularly for highly elliptic orbits such as an NRHO. The spacecraft's uncertainty ellipsoid in the Earth-Moon rotating frame, which is integral to the construction of a Keep-Out Zone (KOZ) or safety domain, is typically elongated along the spacecraft's velocity direction because large velocities magnify the associated positional uncertainty. Nevertheless, such an ellipsoid rotates within the LVLH (or RTN) frame as the spacecraft orbits, presenting geometric challenges.

The goal of this paper is to bridge the research gap between the well-developed studies of bounded relative motion and control in the Perturbed Restricted Two-Body Problem (PR2BP) and those in the CR3BP. Three main contributions are presented in this paper. First, the relative dynamics in the CR3BP are newly derived in the TNW frame ("NTW frame" in Ref. 27, P.159), where two axes are aligned with the spacecraft's velocity and angular momentum in the rotating frame. A QPRO in the TNW frame yields a compact bounded motion, containing large oscillatory behavior only in the velocity direction. This provides an easier understanding of relative motions in the CR3BP compared to a description in the LVLH frame. Secondly, the geometric relationship between the QPRO in the CR3BP and periodic relative orbits in the PR2BP is harmonized in this paper. It is shown that the local eigenspace associated with the periodic orbit in the Earth-Moon rotating frame defines the geometric configuration of the quasi-periodic relative motion. Furthermore, insights into the minimum separation in relevant projections of the co-moving local frames are provided. Finally, an optimal control problem (OCP) is solved in the LTC for the first time. Leveraging this state representation offers a simple yet effective constraint of passive safety with a geometric intuition.

The remainder of the paper is organized as follows. First, nonlinear and linear equations of relative motion

for the CR3BP in the TNW frame are derived. The derivation of the LTC is also revisited. Secondly, the passive safety of the quasi-periodic relative motion is examined in relation to the relative orbit design in the PR2BP. Third, using the invariance property of the local toroidal coordinates, an OCP is formulated as a nonconvex optimization problem and solved by Sequential Convex Programming (SCP). Furthermore, the results of the OCPs are validated with high-fidelity dynamics models. Finally, conclusions and future research directions are provided.

DYNAMICS AND STATE REPRESENTATION

The following notations are used in this paper. For a vector $\boldsymbol{\zeta}$, $\zeta = \|\boldsymbol{\zeta}\|$ denotes an l_2 norm. A vector with a $\hat{\boldsymbol{\zeta}}$ indicates a unit vector. $[\boldsymbol{\zeta}]^\times$ denotes a skew-symmetric matrix that provides a cross product ($\boldsymbol{\zeta}\times$). The first, second, and third-order time derivatives are denoted as $\dot{\boldsymbol{\zeta}} = \partial\boldsymbol{\zeta}/\partial t$, $\ddot{\boldsymbol{\zeta}} = \partial^2\boldsymbol{\zeta}/\partial t^2$, and $\dddot{\boldsymbol{\zeta}} = \partial^3\boldsymbol{\zeta}/\partial t^3$, respectively. A vector expressed in frame $\mathcal{A}$ is denoted as $[\boldsymbol{\zeta}]_\mathcal{A}$. $\mathrm{diag}(\boldsymbol{\zeta})$ represents a diagonal matrix with diagonal entries corresponding to the elements of $\boldsymbol{\zeta}$. An angular velocity of A relative to B is denoted as $\boldsymbol{\omega}_{A/B}$. The operator $\because$ is a shorthand sign for "because". The d-dimensional real space is denoted as $\mathbb{R}^d$, and the d-dimensional toroidal space is denoted as $\mathbb{T}^d$.

This paper considers a system comprising two spacecraft, the chief and the deputy, operating near the Moon and influenced by the gravitational forces of both the Earth and the Moon. Particularly, CR3BP assumes that the spacecraft's mass is negligible compared to that of the Earth and the Moon, and that the two celestial bodies revolve in circular orbits around their barycenter. The absolute positions of the chief and deputy from the Moon's center of mass are denoted as $\boldsymbol{r}$ and $\boldsymbol{r}_d$, respectively. The relative position of the deputy spacecraft with respect to the chief is expressed as $\boldsymbol{\rho} = \boldsymbol{r}_d - \boldsymbol{r}$.

Coordinate Frames

Absolute Frames The coordinate frames that are used in this paper are summarized in Figure 1. Figure 1a illustrates the absolute coordinate frames: inertial frame, barycenter synodic frame, and Moon synodic frame. The barycenter synodic frame is a rotating frame about the Earth-Moon barycenter B_1. The Moon synodic frame is attached to the barycenter synodic frame, while the origin of the frame is anchored to the Moon. This frame is useful for expressing states of spacecraft in cislunar orbits. In this paper, an absolute orbit/motion is defined as one that exhibits periodic motion around an attractor (e.g., Earth/Moon's center of mass, libration points, etc.). These orbits/motions are usually resolved in an absolute frame.

Local Frames There are two co-moving coordinate frames that are commonly used to describe the relative motion between spacecraft: LVLH and TNW frames, as shown in Figure 1b. First, the LVLH frame $\mathcal{L}$ is defined by the right-handed triad $\{\hat{\boldsymbol{\imath}}_L, \hat{\boldsymbol{\jmath}}_L, \hat{\boldsymbol{k}}_L\}$ based on the absolute position of the chief spacecraft as

$$\hat{\boldsymbol{\imath}}_L = \hat{\boldsymbol{\jmath}}_L \times \hat{\boldsymbol{k}}_L, \quad \hat{\boldsymbol{\jmath}}_L = -\frac{\boldsymbol{h}}{h}, \quad \hat{\boldsymbol{k}}_L = -\frac{\boldsymbol{r}}{r}. \tag{1}$$

This triad can also define the Radial/Tangential/Normal (RTN) frame $\mathcal{R} : \{-\hat{\boldsymbol{k}}_L, \hat{\boldsymbol{\imath}}_L, -\hat{\boldsymbol{\jmath}}_L\}$. The 2D planes defined using two of these axes are denoted as RT, TN, and RN plane, respectively.

Another way to define a co-moving triad is the TNW frame $\mathcal{V} : \{\hat{\boldsymbol{\imath}}, \hat{\boldsymbol{\jmath}}, \hat{\boldsymbol{k}}\}$, where the unit basis vectors are defined based on the spacecraft velocity as follows:

$$\hat{\boldsymbol{\imath}} = \frac{\boldsymbol{v}}{v}, \quad \hat{\boldsymbol{\jmath}} = \frac{\boldsymbol{h}}{h}, \quad \hat{\boldsymbol{k}} = \hat{\boldsymbol{\imath}} \times \hat{\boldsymbol{\jmath}}. \tag{2}$$

Also, the 2D planes defined using two of these axes are termed TN, TW, and WN plane, respectively. The LVLH frame and the TNW frame coincide in a circular orbit. Similarly to an absolute orbit, a relative orbit/motion is defined as one that exhibits periodic motion around the (virtual) chief spacecraft resolved in its local frames.

For the subscripts of an angular velocity $\boldsymbol{\omega}$ and a vector $[\boldsymbol{\zeta}]$, $v/\mathcal{V}$ denotes the TNW frame, $m/\mathcal{M}$ denotes the Moon synodic frame, and $i/\mathcal{I}$ denotes the inertial frame.

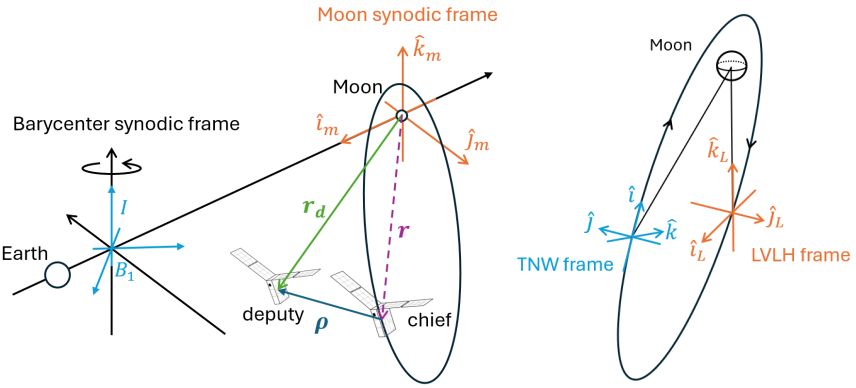

(a) Absolute coordinate frames (b) Local coordinate frames

Figure 1: Coordinate frames and vectors used in this work.

Relative CR3BP dynamics in the TNW frame

Following the derivation of the relative dynamics in CR3BP within the LVLH frame,[13] this subsection develops nonlinear and linear relative dynamics in CR3BP in the TNW frame. While this derivation assumes the CR3BP and the chief spacecraft being anchored to the Moon, the extension to ER3BP[13] and BCR4BP,[15] or orbits around other anchoring points (e.g., libration points) can be easily obtained.[14]

A key difference in the derivation in the TNW frame compared to that in the LVLH frame[13] is the analytical expression of the angular velocity of the TNW frame with respect to the LVLH frame $\boldsymbol{\omega}_{v/m}$ and its time derivative $\dot{\boldsymbol{\omega}}_{v/m}$. This requires a time derivative of basis vectors of the TNW frame which are expressed in the Moon synodic frame. The time derivative of $\hat{\boldsymbol{\imath}}$ is computed as follows:

$$[\dot{\hat{\boldsymbol{\imath}}}]_{\mathcal{M}} = \frac{d}{dt}\left(\frac{[\dot{\boldsymbol{r}}]_{\mathcal{M}}}{v}\right) = \frac{1}{v}([\ddot{\boldsymbol{r}}]_{\mathcal{M}} - \hat{\boldsymbol{\imath}}\cdot(\hat{\boldsymbol{\imath}}\cdot[\dot{\boldsymbol{r}}]_{\mathcal{M}})) \quad \left(\because \dot{v} = \frac{[\dot{\boldsymbol{r}}]_{\mathcal{M}}\cdot[\ddot{\boldsymbol{r}}]_{\mathcal{M}}}{v} = \hat{\boldsymbol{\imath}}\cdot[\ddot{\boldsymbol{r}}]_{\mathcal{M}}\right) \tag{3a}$$

$$= \frac{1}{v}(([\ddot{\boldsymbol{r}}]_{\mathcal{M}}\cdot\hat{\boldsymbol{\jmath}})\hat{\boldsymbol{\jmath}} + ([\ddot{\boldsymbol{r}}]_{\mathcal{M}}\cdot\hat{\boldsymbol{k}})\hat{\boldsymbol{k}}) \tag{3b}$$

$$= \frac{1}{hv}([\ddot{\boldsymbol{r}}]_{\mathcal{M}}\cdot\boldsymbol{h})\hat{\boldsymbol{\jmath}} + \frac{1}{v}([\ddot{\boldsymbol{r}}]_{\mathcal{M}}\cdot\hat{\boldsymbol{k}})\hat{\boldsymbol{k}}. \tag{3c}$$

Using the definition in Eq. (2), the time derivative of $\hat{\boldsymbol{\jmath}}$ is computed as follows:

$$[\dot{\hat{\boldsymbol{\jmath}}}]_{\mathcal{M}} = \frac{1}{h^2}([\dot{\boldsymbol{h}}]_{\mathcal{M}}h - \boldsymbol{h}\dot{h}) \tag{4a}$$

$$= \frac{1}{h}([\dot{\boldsymbol{h}}]_{\mathcal{M}} - \dot{h}\hat{\boldsymbol{\jmath}}) \tag{4b}$$

$$= \frac{1}{h}([\dot{\boldsymbol{h}}]_{\mathcal{M}}\cdot\hat{\boldsymbol{\imath}})\hat{\boldsymbol{\imath}} + \frac{1}{h}([\dot{\boldsymbol{h}}]_{\mathcal{M}}\cdot\hat{\boldsymbol{k}})\hat{\boldsymbol{k}} \tag{4c}$$

$$= -\frac{1}{hv}([\ddot{\boldsymbol{r}}]_{\mathcal{M}}\cdot\boldsymbol{h})\hat{\boldsymbol{\imath}} + \frac{1}{h}([\dot{\boldsymbol{h}}]_{\mathcal{M}}\cdot\hat{\boldsymbol{k}})\hat{\boldsymbol{k}} \tag{4d}$$

From Eq. 4b to 4c, the following equality is used, noting that $[\dot{\boldsymbol{h}}]_{\mathcal{V}} = \dot{h}\hat{\boldsymbol{\jmath}}$:

$$\dot{h} = [\dot{\boldsymbol{h}}]_{\mathcal{V}}\cdot\hat{\boldsymbol{\jmath}} = [\dot{\boldsymbol{h}}]_{\mathcal{M}}\cdot\hat{\boldsymbol{\jmath}} - (\boldsymbol{\omega}_{v/m}\times\boldsymbol{h})\cdot\hat{\boldsymbol{\jmath}} = [\dot{\boldsymbol{h}}]_{\mathcal{M}}\cdot\hat{\boldsymbol{\jmath}}. \quad \left(\because (\boldsymbol{\omega}_{v/m}\times\boldsymbol{h})\cdot\hat{\boldsymbol{\jmath}} = \frac{1}{h}(\boldsymbol{\omega}_{v/m}\times\boldsymbol{h})\cdot\boldsymbol{h} = 0\right) \tag{5a}$$

Also note that $[\dot{\boldsymbol{h}}]_{\mathcal{M}} = \boldsymbol{r}\times[\ddot{\boldsymbol{r}}]_{\mathcal{M}}$. Finally, the time derivative of $\hat{\boldsymbol{k}}$ is computed as follows:

$$[\dot{\hat{\boldsymbol{k}}}]_{\mathcal{M}} = [\dot{\hat{\boldsymbol{\imath}}}]_{\mathcal{M}}\times\hat{\boldsymbol{\jmath}} + \hat{\boldsymbol{\imath}}\times[\dot{\hat{\boldsymbol{\jmath}}}]_{\mathcal{M}} = -\frac{1}{v}([\ddot{\boldsymbol{r}}]_{\mathcal{M}}\cdot\hat{\boldsymbol{k}})\hat{\boldsymbol{\imath}} - \frac{1}{h}([\dot{\boldsymbol{h}}]_{\mathcal{M}}\cdot\hat{\boldsymbol{k}})\hat{\boldsymbol{\jmath}}. \tag{6}$$

The time derivative of unit vectors of the TNW frame expressed in the Moon synodic frame can also be expressed using $\boldsymbol{\omega}_{v/m}$ as follows:

$$[\dot{\hat{\boldsymbol{\imath}}}]_{\mathcal{M}} = \boldsymbol{\omega}_{v/m} \times \hat{\boldsymbol{\imath}}, \quad [\dot{\hat{\boldsymbol{\jmath}}}]_{\mathcal{M}} = \boldsymbol{\omega}_{v/m} \times \hat{\boldsymbol{\jmath}}, \quad [\dot{\hat{\boldsymbol{k}}}]_{\mathcal{M}} = \boldsymbol{\omega}_{v/m} \times \hat{\boldsymbol{k}} \tag{7}$$

Taking a cross product with each unit vector from the left side, the following expression is obtained:

$$\hat{\boldsymbol{\imath}} \times [\dot{\hat{\boldsymbol{\imath}}}]_{\mathcal{M}} = \boldsymbol{\omega}_{v/m} - (\boldsymbol{\omega}_{v/m} \cdot \hat{\boldsymbol{\imath}})\hat{\boldsymbol{\imath}}, \quad \hat{\boldsymbol{\jmath}} \times [\dot{\hat{\boldsymbol{\jmath}}}]_{\mathcal{M}} = \boldsymbol{\omega}_{v/m} - (\boldsymbol{\omega}_{v/m} \cdot \hat{\boldsymbol{\jmath}})\hat{\boldsymbol{\jmath}}, \quad \hat{\boldsymbol{k}} \times [\dot{\hat{\boldsymbol{k}}}]_{\mathcal{M}} = \boldsymbol{\omega}_{v/m} - (\boldsymbol{\omega}_{v/m} \cdot \hat{\boldsymbol{k}})\hat{\boldsymbol{k}}. \tag{8}$$

By summing up the three equations, the following equation is derived:

$$\boldsymbol{\omega}_{v/m} = \frac{1}{2}\left(\hat{\boldsymbol{\imath}} \times [\dot{\hat{\boldsymbol{\imath}}}]_{\mathcal{M}} + \hat{\boldsymbol{\jmath}} \times [\dot{\hat{\boldsymbol{\jmath}}}]_{\mathcal{M}} + \hat{\boldsymbol{k}} \times [\dot{\hat{\boldsymbol{k}}}]_{\mathcal{M}}\right) \tag{9}$$

With Eqs. (3), (4), and (6), the angular velocity $\boldsymbol{\omega}_{v/m}$ is expressed in the TNW frame as follows:

$$\boldsymbol{\omega}_{v/m} = \omega^x_{v/m}\hat{\boldsymbol{\imath}} + \omega^y_{v/m}\hat{\boldsymbol{\jmath}} + \omega^z_{v/m}\hat{\boldsymbol{k}} \tag{10a}$$

$$= \frac{1}{h}([\dot{\boldsymbol{h}}]_{\mathcal{M}} \cdot \hat{\boldsymbol{k}})\hat{\boldsymbol{\imath}} - \frac{1}{v}([\ddot{\boldsymbol{r}}]_{\mathcal{M}} \cdot \hat{\boldsymbol{k}})\hat{\boldsymbol{\jmath}} + \frac{1}{hv}([\ddot{\boldsymbol{r}}]_{\mathcal{M}} \cdot \boldsymbol{h})\hat{\boldsymbol{k}} \tag{10b}$$

$$= \frac{1}{h}((\boldsymbol{r} \times [\ddot{\boldsymbol{r}}]_{\mathcal{M}}) \cdot \hat{\boldsymbol{k}})\hat{\boldsymbol{\imath}} - \frac{1}{v}([\ddot{\boldsymbol{r}}]_{\mathcal{M}} \cdot \hat{\boldsymbol{k}})\hat{\boldsymbol{\jmath}} + \frac{1}{hv}([\ddot{\boldsymbol{r}}]_{\mathcal{M}} \cdot \boldsymbol{h})\hat{\boldsymbol{k}} \tag{10c}$$

The time derivative of each component is computed as follows:

$$\dot{\omega}^x_{v/m} = -\frac{\dot{h}}{h^2}((\boldsymbol{r} \times [\ddot{\boldsymbol{r}}]_{\mathcal{M}}) \cdot \hat{\boldsymbol{k}}) + \frac{1}{h}\left(([\dot{\boldsymbol{r}}]_{\mathcal{M}} \times [\ddot{\boldsymbol{r}}]_{\mathcal{M}}) \cdot \hat{\boldsymbol{k}} + (\boldsymbol{r} \times [\dddot{\boldsymbol{r}}]_{\mathcal{M}}) \cdot \hat{\boldsymbol{k}} + (\boldsymbol{r} \times [\ddot{\boldsymbol{r}}]_{\mathcal{M}}) \cdot [\dot{\hat{\boldsymbol{k}}}]_{\mathcal{M}}\right) \tag{11a}$$

$$\dot{\omega}^y_{v/m} = \frac{\dot{v}}{v^2}([\ddot{\boldsymbol{r}}]_{\mathcal{M}} \cdot \hat{\boldsymbol{k}}) - \frac{1}{v}([\dddot{\boldsymbol{r}}]_{\mathcal{M}} \cdot \hat{\boldsymbol{k}} + [\ddot{\boldsymbol{r}}]_{\mathcal{M}} \cdot [\dot{\hat{\boldsymbol{k}}}]_{\mathcal{M}}) \tag{11b}$$

$$\dot{\omega}^z_{v/m} = \frac{-\dot{h}v - h\dot{v}}{h^2v^2}([\ddot{\boldsymbol{r}}]_{\mathcal{M}} \cdot \boldsymbol{h}) + \frac{1}{hv}([\ddot{\boldsymbol{r}}]_{\mathcal{M}} \cdot \boldsymbol{h}). \tag{11c}$$

For the CR3BP, the acceleration and jerk of the chief in the Moon synodic frame are calculated as follows:

$$[\ddot{\boldsymbol{r}}]_{\mathcal{M}} = -2\boldsymbol{\omega}_{m/i} \times [\dot{\boldsymbol{r}}]_{\mathcal{M}} - \boldsymbol{\omega}_{m/i} \times \left(\boldsymbol{\omega}_{m/i} \times \boldsymbol{r}\right) - \mu\frac{\boldsymbol{r}}{r^3} - (1-\mu)\left(\frac{\boldsymbol{r}_{em} + \boldsymbol{r}}{\|\boldsymbol{r}_{em} + \boldsymbol{r}\|^3} - \frac{\boldsymbol{r}_{em}}{r_{em}^3}\right) \tag{12a}$$

$$[\dddot{\boldsymbol{r}}]_{\mathcal{M}} = -2\boldsymbol{\omega}_{m/i} \times [\ddot{\boldsymbol{r}}]_{\mathcal{M}} - \boldsymbol{\omega}_{m/i} \times \left(\boldsymbol{\omega}_{m/i} \times [\dot{\boldsymbol{r}}]_{\mathcal{M}}\right) - \mu\frac{\partial}{\partial \boldsymbol{r}}\left[\frac{\boldsymbol{r}}{r^3}\right][\dot{\boldsymbol{r}}]_{\mathcal{M}} - (1-\mu)\frac{\partial}{\partial \boldsymbol{r}}\left[\frac{\boldsymbol{r}_{em} + \boldsymbol{r}}{\|\boldsymbol{r}_{em} + \boldsymbol{r}\|^3}\right][\dot{\boldsymbol{r}}]_{\mathcal{M}}, \tag{12b}$$

where $\boldsymbol{r}_{em}$ is the position vector from Earth to the Moon, and for a vector $\boldsymbol{\zeta}$,

$$\frac{\partial}{\partial \boldsymbol{\zeta}}\left[\frac{\boldsymbol{\zeta}}{\zeta^3}\right] = \frac{1}{\zeta^3}\left(\boldsymbol{I}_3 - 3\frac{\boldsymbol{\zeta}\boldsymbol{\zeta}^\top}{\zeta^2}\right). \tag{13}$$

After obtaining the angular velocity of the TNW frame with respect to the Moon synodic frame and its derivative, the remaining derivation is identical to Ref. 13. The (exact) nonlinear equation of motion for the relative motion in the CR3BP is described as follows:

$$\begin{aligned}[\ddot{\boldsymbol{\rho}}]_{\mathcal{V}} = &-2[\boldsymbol{\omega}_{v/i}]^\times_{\mathcal{V}}[\dot{\boldsymbol{\rho}}]_{\mathcal{V}} - \left([\dot{\boldsymbol{\omega}}_{v/i}]^\times_{\mathcal{V}} + \left([\boldsymbol{\omega}_{v/i}]^\times_{\mathcal{V}}\right)^2\right)\boldsymbol{\rho} \\ &+ \mu\left(\frac{\boldsymbol{r}}{r^3} - \frac{\boldsymbol{r} + \boldsymbol{\rho}}{\|\boldsymbol{r} + \boldsymbol{\rho}\|^3}\right) + (1-\mu)\left(\frac{\boldsymbol{r}_{em} + \boldsymbol{r}}{\|\boldsymbol{r}_{em} + \boldsymbol{r}\|^3} - \frac{\boldsymbol{r}_{em} + \boldsymbol{r} + \boldsymbol{\rho}}{\|\boldsymbol{r}_{em} + \boldsymbol{r} + \boldsymbol{\rho}\|^3}\right)\end{aligned} \tag{14}$$

By linearizing Eq. 14 around the chief's position, the gravitational accelerations can be formulated as a linear expression of the relative position. Therefore, the linear dynamics can be written in state-space form as

$$\dot{\boldsymbol{x}} = \boldsymbol{A}(\boldsymbol{r}(t))\boldsymbol{x} = \begin{bmatrix} \boldsymbol{0}_3 & \boldsymbol{I}_3 \\ \boldsymbol{A}_{\dot{\boldsymbol{\rho}}\boldsymbol{\rho}} & -2[\boldsymbol{\omega}_{v/i}]^\times \end{bmatrix}\boldsymbol{x}, \quad \boldsymbol{x} = \begin{bmatrix} \boldsymbol{\rho} \\ [\dot{\boldsymbol{\rho}}]_{\mathcal{V}} \end{bmatrix} \tag{15a}$$

$$\text{where} \quad \boldsymbol{A}_{\dot{\boldsymbol{\rho}}\boldsymbol{\rho}} = -[\dot{\boldsymbol{\omega}}_{v/i}]^\times_{\mathcal{V}} - \left([\dot{\boldsymbol{\omega}}_{v/i}]^\times_{\mathcal{V}}\right)^2 - \mu\frac{\partial}{\partial \boldsymbol{r}}\left[\frac{\boldsymbol{r}}{r^3}\right] - (1-\mu)\frac{\partial}{\partial \boldsymbol{r}}\left[\frac{\boldsymbol{r} + \boldsymbol{r}_{em}}{\|\boldsymbol{r} + \boldsymbol{r}_{em}\|^3}\right] \tag{15b}$$

Note that $\boldsymbol{\omega}_{v/i} = \boldsymbol{\omega}_{v/m} + \boldsymbol{\omega}_{m/i}$ and $[\dot{\boldsymbol{\omega}}_{v/i}]_{\mathcal{V}} = [\dot{\boldsymbol{\omega}}_{v/m}]_{\mathcal{V}} - \boldsymbol{\omega}_{v/m} \times \hat{\boldsymbol{k}}_m$.[13]

Quasi-Periodic Invariant Tori: From the Perspective of a Nonlinear Dynamical System

Bounded periodic relative motion in the R2BP is driven by two periodic absolute motions as shown in Figure 2a. In contrast, bounded quasi-periodic relative motion in the CR3BP leverages a QPIT as presented in Figure 2b.

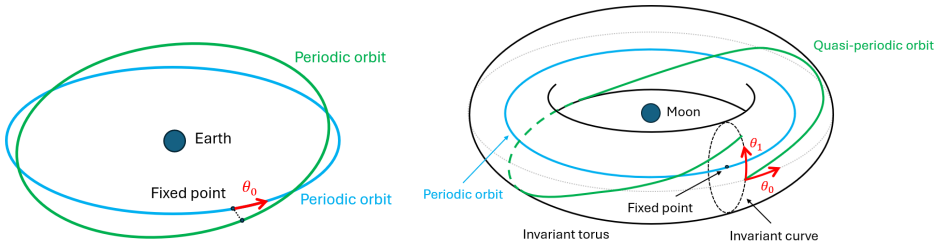

(a) Periodic orbits around Earth characterized by one-dimensional torus $\mathbb{T}$

(b) Two-dimensional ($\mathbb{T}^2$) quasi-periodic invariant torus and a quasi-periodic orbit

Figure 2: Periodic and quasi-periodic absolute motion in the P2BP and CR3BP.

In a Hamiltonian dynamical system, an invariant torus is a stable geometric structure along which solutions evolve without altering their overall shape. This bounded motion is realized because a point on its surface follows the vector field of the system's equations of motion. Any position and velocity ($\mathbb{R}^6$) on its surface can be characterized by a d-dimensional of toroidal vector $\boldsymbol{\theta} \in \mathbb{T}^d$, also called a phase vector. Therefore, the evolution of natural motion, when initialized at a point on the torus, can be expressed as an evolution of $\boldsymbol{\theta}$. As shown in Figure 2a, a periodic absolute orbit is indeed a one-dimensional torus, parameterized by $\boldsymbol{\theta} = \theta_0 \in \mathbb{T}$. In the CR3BP, there exist periodic absolute orbits that have a corresponding two-dimensional invariant torus, characterized by $\boldsymbol{\theta} = [\theta_0, \theta_1] \in \mathbb{T}^2$. As shown in Figure 2b, θ_0 represents the phase along a periodic absolute orbit with a period of T, while θ_1 is defined as the phase within an invariant curve. An invariant curve is a closed curve where points map onto themselves under the T-stroboscopic map. If θ_1 makes an angular displacement after θ_0 completes a full rotation, this motion is called a bounded "quasi-"periodic motion on a QPO instead of periodic motion. The corresponding invariant torus is defined as a two-dimensional QPIT.

For the CR3BP, a QPO and a QPIT can be found as an equilibrium in a rotating frame, enveloping the corresponding periodic orbit without an intersection. As shown in Figure 2b, a spacecraft on a QPO performs not only a quasi-periodic bounded motion with respect to the attractor (e.g., Moon) in the rotating frame but also a quasi-periodic bounded relative motion in a local frame on the periodic orbit. Therefore, a QPRO and QPRIT can be reconstructed by mapping the QPO and QPIT from the rotating frame to the chief's local frame. Note that a QPRIT can also be constructed directly from the relative dynamics in the local frame. That is, a QPIT generated from the relative dynamics in the local frame coincides with the QPRIT.

Periodic and Quasi-Periodic Relative Motion: From the Perspective of a Linear Dynamical System

From the perspective of the linear dynamical system, periodic relative motion in the R2BP and quasi-periodic relative motion in the CR3BP can also be derived by analyzing the eigensystem of the local monodromy matrix associated with the respective linear dynamics.

First, a complete periodic relative orbit to an absolute orbit of the R2BP arises because all six eigenvalues of the monodromy matrix are one. The dynamical mode associated with this eigenvalue is called the central mode. For example, the monodromy matrix of the HCW equation[1] resolved in the RTN frame is given as

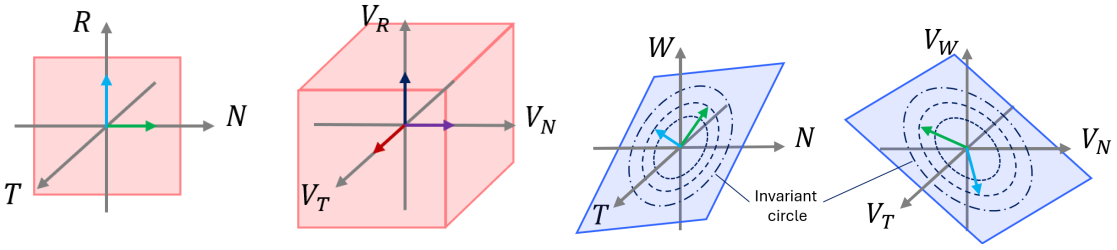

(a) Central mode in the relative motion of the R2BP. (b) Oscillatory mode in the relative motion of the CR3BP.

Figure 3: Local eigenspace of the monodromy matrix: central mode in the R2BP and the oscillatory mode in the CR3BP.

follows:

$$M_{HCW} = \begin{bmatrix} 1 & -12\pi & 0 & 0 & 0 & 0 \\ 0 & 1 & 0 & 0 & 0 & 0 \\ 0 & 0 & 1 & 0 & 0 & 0 \\ 0 & 0 & 0 & 1 & 0 & 0 \\ 0 & -6\pi/n & 0 & 0 & 1 & 0 \\ 0 & 0 & 0 & 0 & 0 & 1 \end{bmatrix}, \tag{16}$$

where n denotes the mean motion. The five unique eigenvectors (corresponding to the central mode) are unit vectors of all six directions except for a mode in the along-track direction, as shown in Figure 3a. This eigensystem implies that any initial condition results in periodic relative motion, except for the along-track direction. This component exhibits drift in the case of differences in specific mechanical energy (or semi-major axis) as approximated by the linearization.[3] When additional perturbations are considered (i.e., PR2BP), some eigenvalues of the monodromy matrix perturb from one. Thus, the solution set for periodic relative motion becomes smaller due to the additional conditions required for periodicity. For example, previous works[3,28] address relative orbit designs that cancel a secular drift caused by the J_2-perturbation.

In the HCW equation, the linearized equations about a reference orbit have constant coefficients, allowing an analytic solution for the monodromy matrix. In contrast, the CR3BP retains time-varying nonlinearity even under local linearization, preventing a closed-form monodromy matrix. Instead, numerical integration is a common approach. Since the plant matrix $\boldsymbol{A}(t)$ in Eq. (15) is a function of the chief's absolute position and velocity, the monodromy matrix is computed by concurrently propagating the STM Φ and the chief's absolute motion for the time interval $[t_0, t_0 + T]$:

$$\begin{cases} [\dot{\boldsymbol{y}}(t)]_{\mathcal{M}} & = \begin{bmatrix} [\dot{\boldsymbol{r}}]_{\mathcal{M}} \\ [\ddot{\boldsymbol{r}}]_{\mathcal{M}} \end{bmatrix}, \quad \boldsymbol{y} = \begin{bmatrix} \boldsymbol{r} \\ \dot{\boldsymbol{r}} \end{bmatrix}, \quad [\boldsymbol{y}(t_0)]_{\mathcal{M}} = \begin{bmatrix} [\boldsymbol{r}_0]_{\mathcal{M}} \\ [\dot{\boldsymbol{r}}_0]_{\mathcal{M}} \end{bmatrix} \\ \dot{\Phi}(t_0, t_0 + t) & = A(\boldsymbol{r}(t))\Phi(t_0, t_0 + t), \quad \Phi(t_0, t_0) = \boldsymbol{I}_6. \end{cases} \tag{17}$$

This system is a 42-dimensional ordinary differential equation. Note that the chief's acceleration is obtained from Eq. (12a). Generally, not all eigenvalues of the monodromy matrix computed by Eq. (17) are one. Therefore, the set of periodic solutions for the relative motion is severely constrained; a trivial solution involves relative motion between spacecraft on the same periodic absolute orbit but with phase offsets. However, it is known that for some periodic orbits, the monodromy matrix contains an oscillatory mode, which is associated with a pair of complex unit-norm eigenvalues.[11,22] An initial relative position and velocity within the corresponding eigenspace result in a quasi-periodic motion, where the relative position and velocity vectors rotate along the circumference of an ellipse called an invariant circle (illustrated as dotted ellipses in Figure 3b) on the eigenspace after each absolute orbit. Furthermore, the eigenvalue also determines this rotation angle in each absolute orbit, defined as a rotation number.[29,30]

It is known that the quasi-periodic relative motion constructed based on the oscillatory mode is the first-order approximation of the QPO in a local frame.[19] Evidently, the invariant circle is a first-order approximation of the invariant curve in Figure 2b that is resolved in a local frame.[29] Furthermore, the phase drift on the

invariant circle that is caused by the oscillatory mode (cf. Fig. 3b) is the first-order approximation of the drift in θ_1 on the invariant curve (cf. Fig. 2b).

While the PR2BP allows substantial design flexibility for relative orbit configurations, the design of quasi-periodic relative motion exploiting the oscillatory mode is heavily constrained, being inherently dictated by the chief's absolute orbit and its associated local eigenspace. This can be also confirmed from the nonlinear dynamics (cf. Figure 2), where the relative orbit design in the CR3BP is fundamentally equivalent to the QPIT design with a given periodic absolute orbit.

Local Toroidal Coordinates

Numerical computation of a QPIT with nonlinear dynamics has been expensive for onboard applications.[29,30] To overcome this limitation, the LTC[22] has been introduced to describe a relative motion using the local eigenspace of a periodic absolute orbit. As mentioned, the existence of a QPRO relies on the presence of an oscillatory mode in the monodromy matrix, associated with a pair of complex unit-norm eigenvalues. It is assumed in this paper that the chief is on a periodic orbit of the CR3BP that contains at least one oscillatory mode in its monodromy matrix. Figure 4 illustrates the local eigenspace for the oscillatory mode at a certain phase in the chief's orbit (also known as a fixed point that serves as the initial point of the integration of the monodromy matrix). Using the local eigenspace, an osculating invariant circle is expressed as follows:[29]

$$\boldsymbol{\psi}(t) = \varepsilon \left(\mathrm{Re}(\boldsymbol{w}(t)) \cos\theta + \mathrm{Im}(\boldsymbol{w}(t)) \sin\theta \right), \tag{18}$$

where $\boldsymbol{w}(t) = \boldsymbol{w}_r(t) + \boldsymbol{w}_i(t)i$ is the eigenvector for the oscillatory mode of the monodromy matrix at the

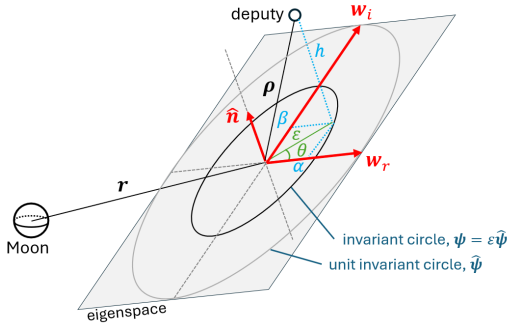

Figure 4: Nonsingular local toroidal coordinates $[\alpha, \beta, h]$ and geometric local toroidal coordinates $[\varepsilon, \theta, h]$

fixed point. Note that the eigenvalues of the monodromy matrix are invariant to the fixed point on a periodic orbit, although the corresponding eigenvectors vary depending on the chosen fixed point. Furthermore, ε is a scaling parameter that defines the size of the invariant curve, and θ (cf. equivalent to θ_1 in Figure 2b) defines a phase in the invariant circle. Note that Eq. (18) implies that there exists only one design variable (ε) in terms of the shape of the invariant circle, given a fixed point.

The complex eigenvector $\boldsymbol{w}(t)$ can also be written in a position and velocity component as follows:

$$\boldsymbol{w}(t) = \boldsymbol{w}_r(t) + \boldsymbol{w}_i(t)i = \begin{bmatrix} \boldsymbol{r}_r(t) \\ \boldsymbol{v}_r(t) \end{bmatrix} + \begin{bmatrix} \boldsymbol{r}_i(t) \\ \boldsymbol{v}_i(t) \end{bmatrix} i, \quad \boldsymbol{r}_r(t) = \begin{bmatrix} c_1(t) \\ c_3(t) \\ c_5(t) \end{bmatrix}, \quad \boldsymbol{r}_i(t) = \begin{bmatrix} c_2(t) \\ c_4(t) \\ c_6(t) \end{bmatrix}. \tag{19}$$

Using this nomenclature, the unit normal vector to the local eigenspace spanned by $\boldsymbol{r}_r$ and $\boldsymbol{r}_i$ is defined as $\hat{\boldsymbol{n}}(t) = (\boldsymbol{r}_r(t) \times \boldsymbol{r}_i(t))/\|\boldsymbol{r}_r(t) \times \boldsymbol{r}_i(t)\|$.

Normalization and sign checks are necessary to achieve a consistent representation of the eigenvector and to construct a triad from the local eigensystem. First, Singular Value Decomposition (SVD) provides the principal axes of the ellipse in Eq. (18). Let $\boldsymbol{w}^*$ denote a complex eigenvector corresponding to the oscillatory

mode of the monodromy matrix that is computed at a fixed point. An SVD to a matrix $\boldsymbol{E} = [\boldsymbol{w}_r^*, \boldsymbol{w}_i^*] \in \mathbb{R}^{6\times 2}$ yields $\boldsymbol{E} = \boldsymbol{U}\boldsymbol{\Sigma}\boldsymbol{V}^\top$, where $\boldsymbol{U} \in \mathbb{R}^{6\times 2}$ is semi-orthogonal, $\boldsymbol{\Sigma} \in \mathbb{R}^{2\times 2}$ is diagonal, and $\boldsymbol{V} \in \mathbb{R}^{2\times 2}$ is orthogonal. Then, two columns of $\boldsymbol{E}\boldsymbol{V} = \boldsymbol{U}\boldsymbol{\Sigma} = [\boldsymbol{w}_r, \boldsymbol{w}_i]$ becomes orthogonal, expressing the principal axes of the invariant circle with the eigenvector $\boldsymbol{w} = \boldsymbol{w}_r + \boldsymbol{w}_i i$. Additionally, to specify the size of the complex eigenvector, it is normalized so that the real, position component $\boldsymbol{r}_r$ becomes a unit vector. Finally, the remaining sign ambiguity of the resulting pair of vectors $\{\boldsymbol{r}_r, \boldsymbol{r}_i, \hat{\boldsymbol{n}}\}$ is resolved.[19] First, if $\hat{\boldsymbol{n}}^\top \hat{\boldsymbol{k}} < 0$, then the conjugate of $\boldsymbol{w}$ is taken. Additionally, if $[1, 1, 0]^\top \hat{\boldsymbol{r}}_r < 0$, then the negative of $\boldsymbol{w}$ is used. Note that other processes can be taken to make the eigenvector direction unique. The above process provides a unique triad $\{\boldsymbol{r}_r, \boldsymbol{r}_i, \hat{\boldsymbol{n}}\}$, which is a set of basis vectors of local toroidal coordinates at a given fixed point. Note that the defined triad (i.e., the complex eigenvector $\boldsymbol{w}$) is time-varying and is a function of the chief's absolute motion. Once normalized at the fixed point, the evolution of $\boldsymbol{w}$ can be computed by the linear dynamics

$$\dot{\boldsymbol{w}}(t) = \boldsymbol{A}(t)\boldsymbol{w}(t), \tag{20}$$

where the plant matrix is obtained from Eq. (15). Therefore, the triad $\{\boldsymbol{r}_r, \boldsymbol{r}_i, \hat{\boldsymbol{n}}\}$ is generally not orthogonal except for the initial triad at the fixed point.

Within the local toroidal frame, the relative position of the deputy to the chief is written as $\boldsymbol{\rho} = \alpha\boldsymbol{r}_r + \beta\boldsymbol{r}_i + h\hat{\boldsymbol{n}}$. Based on this, nonsingular LTC is defined as $\boldsymbol{\zeta}_{\text{ns}} := [\alpha, \beta, h, \dot{\alpha}, \dot{\beta}, \dot{h}]^\top$, where time derivatives are taken in the local toroidal frame. The exact mapping from the nonsingular LTC $\boldsymbol{\zeta}_{\text{ns}}$ to the relative position and velocity expressed in the Cartesian frame $\boldsymbol{\rho}$ is related by the matrix $T(t)$ as follows:

$$\boldsymbol{\rho} = T(t)\boldsymbol{\zeta}_{\text{ns}}, \quad T(t) := \begin{bmatrix} R(t) & \boldsymbol{0}_3 \\ R'(t) & R(t) \end{bmatrix}, \tag{21}$$

where $R(t) := [\boldsymbol{r}_r(t), \boldsymbol{r}_i(t), \hat{\boldsymbol{n}}(t)]$ and $R'(t) := [\boldsymbol{v}_r(t), \boldsymbol{v}_i(t), \dot{\hat{\boldsymbol{n}}}(t)]$. The time derivative of the unit normal vector $\dot{\hat{\boldsymbol{n}}}(t)$ is computed as follows:

$$\dot{\hat{\boldsymbol{n}}}(t) = (\boldsymbol{v}_r(t) \times \boldsymbol{r}_i(t) + \boldsymbol{r}_r(t) \times \boldsymbol{v}_i(t)) - (\boldsymbol{n}(t)^\top (\boldsymbol{v}_r(t) \times \boldsymbol{r}_i(t) + \boldsymbol{r}_r(t) \times \boldsymbol{v}_i(t)))\boldsymbol{n}(t). \tag{22}$$

One can also define LTC by expressing the eigenspace component in polar coordinates (cf. Eq. (18)) as $\boldsymbol{\zeta}_{\text{geo}} := [\varepsilon, \theta, h, \dot{\varepsilon}, \dot{\theta}, \dot{h}]^\top$, which is called as geometric LTC. A similar mapping from the geometric LTC to Cartesian coordinates is available,[19] although the transformation is no longer a function of only the chief's motion but also a time derivative of nonsingular LTC.

The first-order condition to be on a QPRIT (and therefore, being on a corresponding QPRO) is to stay on the eigenspace spanned by $\boldsymbol{w}_r(t)$ and $\boldsymbol{w}_i(t)$. This leads to the condition $h = \dot{\alpha} = \dot{\beta} = \dot{h} = 0$, or in the geometric LTC, $h = \dot{\varepsilon} = \dot{\theta} = \dot{h} = 0$.[22] Any other coordinates still define the deputy's relative motion, although the quasi-periodicity is no longer attainable. The quasi-periodic condition allows for arbitrary choices of the variables (α, β) (or (ε, θ)), defining both the size of the invariant circle and its phase. However, nonzero values in $(\dot{\alpha}, \dot{\beta})$ (or $(\dot{\varepsilon}, \dot{\theta})$) result in a drift in the h-component. Therefore, these parameters must be constant to stay on the QPRIT and maintain the quasi-periodicity.

SAFETY EVALUATION OF THE QPIT

Although the approach is general, the application case of this paper is on the 9:2 South NRHO, which has an orbital period of 6.5 days. This specific choice is due to its practical interest in mission design in cislunar space such as lunar Gateway.[31,32] Figures 5a and 5b illustrate the first-order approximation of a QPRIT resolved in the LVLH and TNW frame, respectively. The surface of the QPRIT is generated by the continuation of invariant circles (cf. Eq. (18)) along the chief's orbit, shown as a gray surface. Additionally, 50 osculating invariant circles are sampled at uniform time intervals over an absolute orbital period and depicted as blue ellipses. Both figures represent the same QPRIT, where the initial fixed point is anchored to the apolune and a scaling factor $\varepsilon = 200$ m is used. Evidently, the perspective from the TNW frame offers a more compact structure of the QPRIT because the semimajor axis direction of invariant circles aligns with the chief's velocity direction. In highly eccentric orbits like NRHOs, the disparity between the two figures

highlights the angular offset between the LVLH and TNW frame. Previous research[19,22] reports a QPRIT structure characterized by two distinct "circular disks" within cislunar periodic orbit families. It is shown that this is attributed to deviations in the along-track direction from the unit vector $\hat{\boldsymbol{i}}_L$ of the LVLH frame.

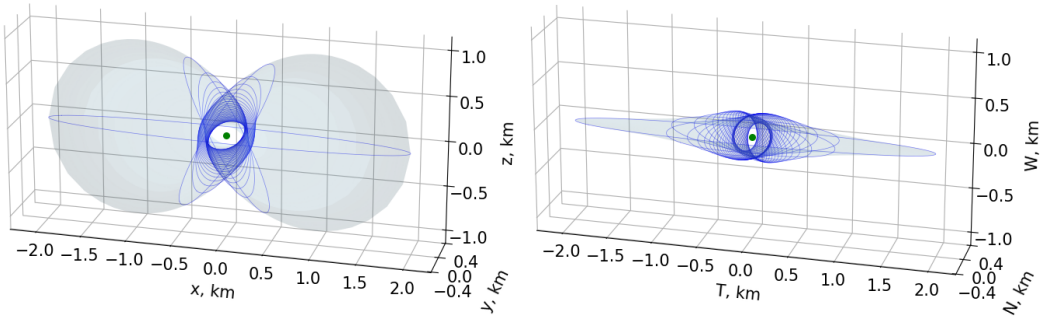

(a) LVLH frame

(b) TNW frame

Figure 5: First-order QPRIT (gray surface) and invariant circles (blue ellipses) in local frames (ε=200 m, fixed point at apolune).

The geometrical structure of cislunar QPROs in a local frame has been well studied.[19] However, previous investigations into the safety of these QPROs have been limited to analysis of the minimum separation and the semi-axes of invariant circles. For bounded relative motion about an orbit in the PR2BP, separation in the Radial/Tangential (RT) and Radial/Normal (RN) plane provided useful insight for the relative orbit design because these separations can effectively encapsulate the three-dimensional uncertainty ellipsoid that is caused by dynamics (process noise), navigation, and actuation errors. A similar approach is taken in this section via a characterization of the osculating invariant circle. Note that the geometry of the osculating relative ellipse is defined by six independent variables (e.g., ROE), whereas the geometric structure of the first-order QPRO in the CR3BP is solely dependent on the chief's absolute orbit with its design space limited to its size (ε, cf. Eq. (18)). Therefore, a "unit" invariant circle $\hat{\boldsymbol{\psi}}$ with $\varepsilon = 1$ could provide a comprehensive geometric property of QPROs.

Connection to Relative Orbital Elements Theory

Figures 6a and 6b illustrate two-dimensional projections of a three-dimensional (osculating) relative orbit in the R2BP and an osculating unit invariant circle in the CR3BP, respectively. For a relative motion around a Keplerian orbit, a six-dimensional variable $\boldsymbol{\kappa} = [\kappa_1, \kappa_2, \kappa_3, \kappa_4, \kappa_5, \kappa_6] \in \mathbb{R}^6$ parameterizes a relative orbit of the deputy spacecraft with respect to the chief, with the additional independent variable $\rho(t) = 1 + e\cos\nu(t)$, where e and $\nu(t)$ denote the eccentricity and the true anomaly of the chief, respectively. In this paper, $\boldsymbol{\kappa}$ denotes the quasi-nonsingular ROE in near-circular orbits[3] and its extension to elliptic orbits.[33] These variables correspond to integration constants of the HCW or YA equations in near-circular and eccentric orbits, respectively. In Figure 6a, $\kappa_1 = 0$ is assumed to realize a non-drifting bounded relative motion.

With the notation in Eq. (19), the osculating invariant circle in Eq. (18) can be rewritten as follows:

$$\boldsymbol{\psi}(t) = \varepsilon \begin{bmatrix} \sqrt{c_1^2(t) + c_2^2(t)}\sin(\theta + \phi_x(t)) \\ \sqrt{c_3^2(t) + c_4^2(t)}\sin(\theta + \phi_y(t)) \\ \sqrt{c_5^2(t) + c_6^2(t)}\sin(\theta + \phi_z(t)) \end{bmatrix}, \quad \begin{cases} \tan\phi_x(t) = c_1(t)/c_2(t) \\ \tan\phi_y(t) = c_3(t)/c_4(t) \\ \tan\phi_z(t) = c_5(t)/c_6(t) \end{cases}. \tag{23}$$

Vectors $[c_1(t), c_2(t)]$, $[c_3(t), c_4(t)]$, and $[c_5(t), c_6(t)]$ provide the amplitudes of the projected ellipse in each plane as well as the oscillation phase. In a relative motion in a Keplerian orbit, these vectors are time-invariant* and correspond to the integration constants $\boldsymbol{\kappa}$. The minimum separation of a projected ellipse in each two-dimensional plane depends on only these three constant vectors, which leads to the well-known

*When adding perturbations (e.g., spherical harmonics, drag, etc.) to the Keplerian dynamics, the osculating ROE also experiences

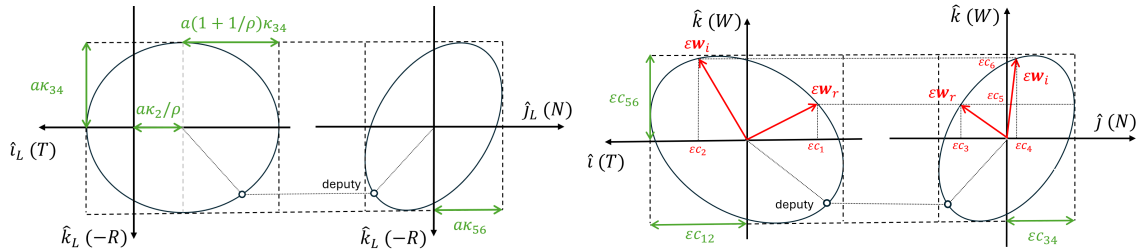

(a) Osculating relative ellipse of a relative orbit (PR2BP, κ_1=0) in the LVLH frame.

(b) Osculating invariant circle of a QPRO (CR3BP) in the TNW frame.

Figure 6: Comparison of the geometric parametrization of osculating relative orbit in the PR2BP and the invariant circle in the CR3BP.

relative eccentricity and inclination vector separation in ROE theory.[3] In contrast, the three vectors are time-varying in the CR3BP, and the amplitude of osculation is not negligible within a single orbital period. Consequently, a combined analysis of the magnitudes and phases along the absolute periodic orbit is necessary to assess passive safety of a QPRO.

The evolution of these vectors (i.e., the eigenvector $\boldsymbol{w}(t)$) that are propagated along the linear dynamics for eight absolute orbital periods is plotted in Figure 7. The traces are resolved in the LVLH frame (Figure 7a) and the TNW frame (Figure 7b), respectively. The segment in the first absolute orbital period is colored orange. Figure 7 is analogous to the plots of the vector fields of relative eccentricity $[\kappa_3, \kappa_4]$ and inclination $[\kappa_5, \kappa_6]$ in the quasi-nonsingular ROE[3,33] because the magnitude of each vector represents the amplitude of osculating invariant circle in each direction of the axis (c_{12}, c_{34}, and c_{56}), and the magnitudes of the two vectors and the phase difference between them determine the minimum separation in the corresponding two-dimensional projected plane. However, note again that the vectors $[c_1(t), c_2(t)]$, $[c_3(t), c_4(t)]$, and $[c_5(t), c_6(t)]$ for a unit invariant circle are determined by the local eigensystem of the chief's absolute position and velocity, whereas the relative eccentricity and inclination vectors are free design variables of the deputy.

From each vector field illustrated in Figure 7, a quasi-periodic behavior is confirmed with a drastic change in its amplitude. Note that the equivalent vectors in relative motion for the PR2BP (e.g., ROE or $\boldsymbol{\kappa}$) would be stationary (for a near-circular orbit) or oscillatory about a line segment (for an elliptic orbit), with possible slow secular drifts due to perturbations. The evolution of each vector can be characterized by two angles $\boldsymbol{\theta} = [\theta_0, \theta_1] \in \mathbb{T}^2$. The first angle, θ_0, corresponds to the fixed point in the chief's orbital location, and the second angle, θ_1, is associated with the secular drift of a symmetric axis over multiple orbits. This corresponds to the geometric structure of two-dimensional QPIT and QPRIT (cf. Figure 2b). The angular rate of this secular rotation $\dot{\theta}_1$ remains constant over the three vector fields and corresponds to the angle of the complex eigenvalue of the oscillatory mode, which is uniquely determined by the chief's absolute orbit. For example, an eigenvalue that is associated with the oscillatory mode of the monodromy matrix of the 9:2 South NRHO is $\lambda \simeq 0.715 - 0.699i$, which corresponds to the phase shift (rotation number) of $\tan^{-1}(\mathrm{Im}(\lambda)/\mathrm{Re}(\lambda)) := -44.35°$ per absolute orbit. The displacement between the initial and terminal points of the orange segment illustrates this rotation of θ_1 after one orbit. For both Figures 7a and 7b, the minimum amplitude in the N-direction collapses to nearly zero, as shown in the trace of $[c_3(t), c_4(t)]$. A significant difference between Figures 7a and 7b lies in the vector $[c_5(t), c_6(t)]$, which represents the amplitude of the invariant circle in the R(W)-direction. This is illustrated by the contraction of the amplitude in the W-direction in the TNW frame compared to the R-direction in the LVLH frame.

Additionally, an SVD of the two-dimensional eigenvectors projected on each plane provides information on the amplitudes and minimum separation in three two-dimensional projected planes. Figure 8 illustrates

a drift (although this drift does not induce a (quasi-)periodic motion). However, since the amplitude of the osculation is very small (i.e., the eigenvectors of the monodromy matrix are almost 1), the influence of the perturbation can be treated as a secular drift in an averaged motion over multiple revolutions.

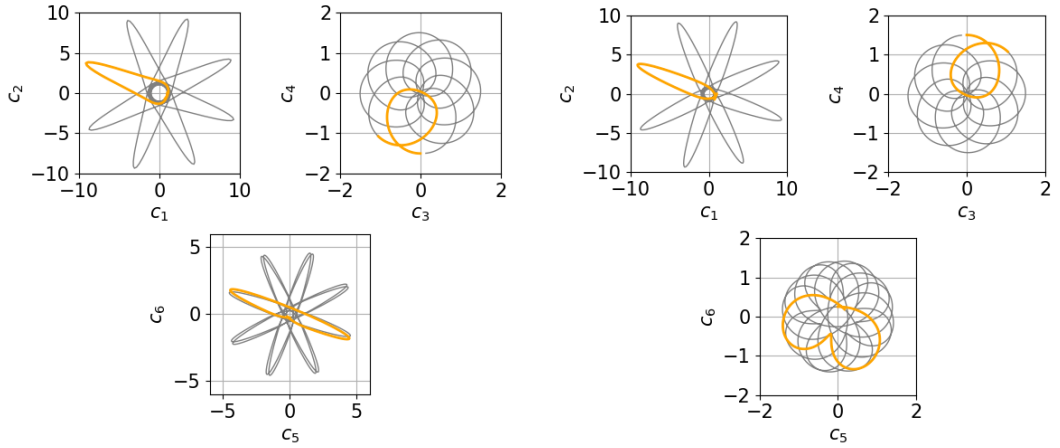

(a) LVLH frame (b) TNW frame

Figure 7: The eight-orbit evolution of $\boldsymbol{r}_r(t)$ and $\boldsymbol{r}_i(t)$. Orange curves correspond to the first orbital period.

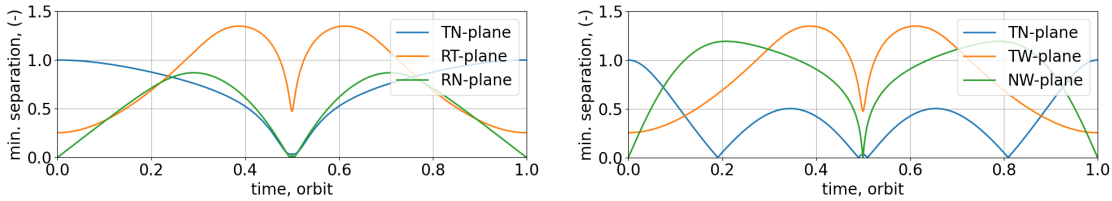

(a) LVLH (RTN) frame (b) TNW frame

Figure 8: Evolution of the minimum planar separation of a unit invariant circle (fixed point: apolune).

the evolution of the minimum separation in each plane of the LVLH (RTN) frame and the TNW frame along an absolute orbit, starting from the apolune. Only the TN plane has a nonzero separation for both frames, whereas TW(RT) and RN(NW) plane separations collapse to zero at the perilune (0.5 orbit). Furthermore, the separation in the TW plane increases by resolving the QPRIT in the TNW frame, whereas additional singularities are generated in the TN plane separation. This leads to a potential passive safety remedy that mostly leverages the TW plane separation in a similar manner to the RN plane separation in relative orbit design in the Keplerian dynamics, while at two apses, these safety criteria are switched to the other planes.

PASSIVELY SAFE RECONFIGURATION USING LOCAL TOROIDAL COORDINATES

Based on the above discussion, an OCP is constructed to provide a passively safe reconfiguration between two QPROs. The discrete-time OCP in the nonsingular LTC is presented as follows:

$$\min_{\{\boldsymbol{\zeta}_{\mathrm{ns},k}\}_{k=0}^{N},\{\boldsymbol{u}_k\}_{k=0}^{N}} \sum_{k=0}^{N} \|\boldsymbol{u}_k\| \tag{24a}$$

$$\text{s.t.} \quad \boldsymbol{\zeta}_{\mathrm{ns},0} = \boldsymbol{\zeta}_{\mathrm{ns},i} + B_0\boldsymbol{u}_0, \quad \boldsymbol{\zeta}_{\mathrm{ns},N} = \boldsymbol{\zeta}_{\mathrm{ns},f} \tag{24b}$$

$$\boldsymbol{\zeta}_{\mathrm{ns},k+1} = A_k\boldsymbol{\zeta}_{\mathrm{ns},k} + B_{k+1}\boldsymbol{u}_{k+1} \qquad k = 0,\ldots,N-1 \tag{24c}$$

$$g_{ps}(\boldsymbol{\zeta}_{\mathrm{ns},k}) \leq 0, \qquad k = 0,\ldots,N \tag{24d}$$

$$\text{where} \quad A_k = T_{k+1}^{-1}\Phi(t_{k+1},t_k)T_k, \quad B_k = \begin{bmatrix} \mathbf{0}_3 \\ R_k^{-1} \end{bmatrix} \tag{24e}$$

The control input is an impulsive velocity change added to the deputy, defined as $\boldsymbol{u}_k = \Delta \boldsymbol{v}_k$ within the TNW frame. The minimum-fuel problem is equivalent to the minimization of the sum of the l_2-norm of the impulsive maneuvers. Using Eq. (21), the control input matrix B_k is derived from the last three columns of T_k^{-1}, which is computed as follows:

$$T^{-1}(t) = \begin{bmatrix} R(t)^{-1} & \mathbf{0}_3 \\ -R(t)^{-1}R'(t)R(t)^{-1} & R(t)^{-1} \end{bmatrix}. \tag{25}$$

Note that the matrix $R_k^{-1} \in \mathbb{R}^{3\times 3}$ is always full rank. Finally, Eq. (24d) presents the passive safety constraint that is applied to each controlled state $\boldsymbol{\zeta}_{\text{ns},k}$, two of which are discussed in the following subsections.

When building a discrete time step around a highly eccentric orbit, a careful design of the epochs is required. This is because the velocity of the spacecraft differs significantly depending on the phase of the orbit, which may lead to singularity and high numerical sensitivity. Therefore, the following time regularization scheme is considered, where the time discretization dt is regularized to a pseudo-time discretization $d\tau$ by a scaling function of the chief's position and velocity as $g(\boldsymbol{y})$ as $dt = g(\boldsymbol{y})d\tau \;\Leftrightarrow\; dt/d\tau = g(\boldsymbol{y})$. This leads to the reformulation of the dynamics in the pseudo-time domain:

$$\frac{d\boldsymbol{y}}{d\tau} = \frac{d\boldsymbol{y}}{dt}\frac{dt}{d\tau} = g(\boldsymbol{y})\dot{\boldsymbol{y}}, \quad \frac{dt}{d\tau} = g(\boldsymbol{y}) \tag{26}$$

A set of regularized time epochs can be determined by propagating the above dynamics over the pseudo-time interval $[\tau_0, \tau_f]$, where the pseudo-time epochs are distributed uniformly. The retrieved time epochs that correspond to the pseudo-time epochs represent a vector of the regularized time epochs. There are numerous works on the selection of the regularization function $g(\boldsymbol{y})$; particularly for the time regularization in the multi-body system, readers are recommended to refer to an extensive comparison made in Ref. 34. In this paper, the well-known Sundman transformation[35] for the two-body system is used, considering that the NRHO is close to an elliptic orbit. The regularization function is defined as $g(\boldsymbol{y}) = r^\alpha$, where r is the distance between the chief spacecraft and the Moon, and $\alpha = 1$ is a user-defined parameter.

Passive Safety via Drift Trajectories From Controlled Nodes

To enforce passive safety during the transfer between QPROs, the following drift-safety constraint is considered based on the natural propagation from the controlled trajectory:[23]

$$\max_{j=0,\ldots,N_{\text{safe}}} \sqrt{\boldsymbol{\rho}_{kj}^\top P \boldsymbol{\rho}_{kj}} - \boldsymbol{\rho}_{kj}^\top P \boldsymbol{\rho}_{kj} \le 0, \quad k = 0, ..., N \tag{27a}$$

$$\text{where} \quad \boldsymbol{\rho}_{kj} = \prod_{l=0}^{j-1} \Phi(t_{l+1}, t_l) T_k \boldsymbol{\zeta}_{\text{ns},k}, \tag{27b}$$

where Eq. (27b) defines the natural propagation of the deputy after each controlled epoch, and Eq. (27a) ensures that the drift trajectory remains outside of the KOZ at each discretized time step. Note that this is an equivalent formulation to the well-known quadratic form of exclusion constraint $\sqrt{\boldsymbol{\rho}^\top P \boldsymbol{\rho}} \ge 1$. In this paper, the KOZ is modeled as an ellipsoid. Its geometric property is characterized by the matrix $P = \text{diag}([1/x_e^2, 1/y_e^2, 1/z_e^2, 0, 0, 0])$, where (x_e, y_e, z_e) are the semi-axes of the ellipsoid in the TNW frame. To prevent the quadratic growth of the number of constraints, the maximum operator is applied over the interval of the drift period $j = 0, ..., N_{\text{safe}}$. Note that an osculating collision avoidance constraint is available by considering only $j = 0$. Since Eq. (27a) is nonconvex, the following convexification is performed with respect to the reference state $\bar{\boldsymbol{\rho}}_k$ as follows:[23,36]

$$-\boldsymbol{a}_k^\top T_k \boldsymbol{\zeta}_{\text{ns},k} + b_k \le 0, \quad k = 0, ..., N \tag{28a}$$

$$\text{where} \quad \boldsymbol{a}_k^\top = \bar{\boldsymbol{\rho}}_k^\top \prod_{l=0}^{j_k^*-1} \Phi(t_{l+1}, t_l) D^\top P D \left(\prod_{l=0}^{j_k^*-1} \Phi(t_{l+1}, t_l) \right)^\top, \quad b_k = \sqrt{\boldsymbol{a}_k^\top \bar{\boldsymbol{\rho}}_k}, \quad D = [\boldsymbol{I}_3, \mathbf{0}_3], \tag{28b}$$

$$j_k^* = \underset{j=0,\ldots,N_{\text{safe}}}{\text{argmax}} \sqrt{\bar{\boldsymbol{\rho}}_{kj}^\top P \bar{\boldsymbol{\rho}}_{kj}} - \bar{\boldsymbol{\rho}}_{kj}^\top P \bar{\boldsymbol{\rho}}_{kj}, \tag{28c}$$

where j_k^* is the time epoch that has the largest violation of the constraint in the drift trajectory emanating from the controlled epoch k, obtained from the previous iteration of the SCP.

Passive Safety via First-Order condition of QPRO

Another method to ensure passive safety during a transfer involves enforcing the first-order condition of remaining on a QPRO. This approach ensures that the deputy always adheres to the surface of a QPRO of arbitrary size (defined by ϵ) while smoothly transitioning between QRPOs, thereby maintaining quasi-periodic motion. The constraint is expressed as follows:

$$\|h_k\| \leq \epsilon_h, \quad \|\dot{h}_k\| \leq \epsilon_{\dot{h}}, \quad \|\dot{\alpha}_k\| \leq \epsilon_{\dot{\alpha}}, \quad \|\dot{\beta}_k\| \leq \epsilon_{\dot{\beta}}, \quad k = 0, ..., N \tag{29a}$$

$$\varepsilon_k = \sqrt{\alpha_k^2 + \beta_k^2} \geq \varepsilon_f, \quad k = 0, ..., N \tag{29b}$$

The deputy's condition to be on a QPRO is $h = \dot{\alpha} = \dot{\beta} = \dot{h} = 0$. However, with the strict form of this equality, the problem would be infeasible as LTC becomes uncontrollable (cf. Eq. (21)). Instead, a set of l_2-norm constraints at each time step is added as shown in Eq. (29a). Furthermore, Eq. (29b) ensures that the deputy is outside of the QPRIT's surface that corresponds to the terminal QPRO. Since the latter constraint is nonconvex, the following convexification is introduced, using the reference state $\bar{\alpha}_k$ and $\bar{\beta}_k$:

$$\varepsilon_f - \frac{1}{\sqrt{\bar{\alpha}_k^2 + \bar{\beta}_k^2}}(\bar{\alpha}_k \alpha_k + \bar{\beta}_k \beta_k) \leq 0, \quad k = 0, ..., N \tag{30}$$

RESULTS AND ANALYSIS

Analysis of the OCP Solutions without Safety Constraints

The control input matrix $B(t)$ that maps an impulsive maneuver, $\Delta \boldsymbol{v}$, to the corresponding variations of LTC is given by Eq. (24e). Unfortunately, it uses $\boldsymbol{w}(t)$ and requires numerical integration of Eq. 20. Thus, deriving analytical control strategies for the LTC directly from the control input matrix becomes challenging.

The practical implementation of analytical and numerical methods for transfers between passively safe relative orbits in the PR2BP often involves phase separation in the relative eccentricity and inclination vector.[3] Notably, solutions to a "plain" OCP, consisting solely of dynamics and boundary conditions, typically demonstrate passive safety by preserving the required separation between the relative eccentricity and inclination vectors.[10] Therefore, before applying the nonconvex passive safety constraints, it is of interest to investigate whether passive safety will be maintained throughout a transfer between (passively safe) QPROs.

A grid search is conducted over various initial and terminal phases of QPROs to investigate trends in transfer cost and the associated safety. The sizes of the initial and terminal QPROs are set to $\varepsilon_i = 500$m and $\varepsilon_f = 200$m, respectively. The transfer time is fixed to two absolute orbits of the NRHO, where the horizon is discretized by $N = 30$. Note that the integer revolution scenario between apolune is preferred as it has the lowest numerical sensitivity. The LTC is defined in the TNW frame, with the boundary phases of the invariant circle (θ_i, θ_f) discretized into 30 uniform intervals within the range of $[0, 2\pi]$. The remaining elements $(h, \dot{h}, \dot{\alpha}, \dot{\beta})$ are set to zero at both boundary conditions to ensure that these states are on the respective QPROs at first-order accuracy. For each grid (θ_i, θ_f), a convex plain OCP problem (cf. Eq. (24) without Eq. (24d)) is solved, and total transfer cost, Δv_{tot}, is obtained from the action history. Moreover, the linear relative dynamics model is used to propagate drift trajectories where collision avoidance and one-period drift safety are evaluated based on Eq. (27a). The configuration of the KOZ is defined to have a stretch in the velocity direction as $(x_e, y_e, z_e) = (200, 95, 95)$m, from which both the initial and terminal QPROs are passively safe. The QPRIT and KOZ are illustrated in Figure 9. The orange ellipse corresponds to the osculating invariant circle at the apolune.

The result of the grid search is summarized in Figure 10. Figure 10a represents the distribution of the total transfer cost Δv_{tot}, and Figures 10b and 10c are the maximum constraint value of collision avoidance and passive safety (i.e., the left-hand side of Eq. (27a)), respectively. Grids encircled by a red rectangle indicate a violation of these safety constraints. Since the passive safety condition includes collision avoidance, the maximum value at each grid in Figure 10b is always larger than the corresponding value in Figure 10c.

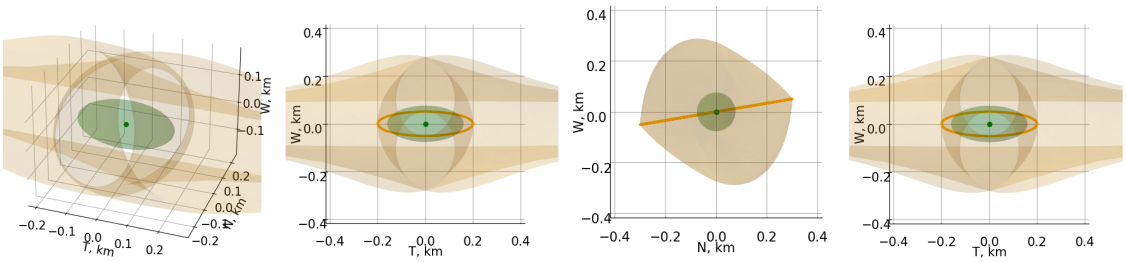

(a) 3D view (b) TN plane projection (c) NW plane projection (d) TW plane projection

Figure 9: The terminal (inner) QPIT (orange) and the keep-out zone (green) in the TNW frame.

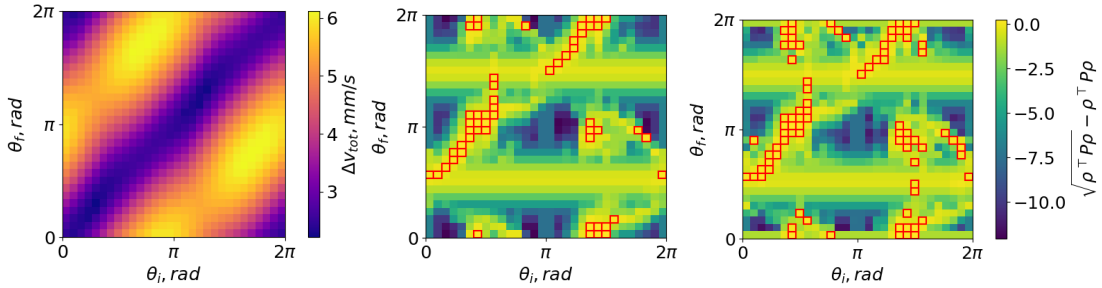

(a) Total transfer cost Δv_{tot} (b) Collision avoidance (c) Passive safety

Figure 10: Δv_{tot} and safety constraint values for different initial/terminal phases in invariant circles.

It is observed that transfers between the same phase are more fuel-efficient, whereas (odd) π phase difference requires larger Δv_{tot}. This corresponds to the invariance of the LTC under the linear relative dynamics. Regarding safety criteria, most fuel-optimal solutions are confirmed to retain a one-orbit passive safety, while some cases violate the constraints. Besides, $\theta_0, \theta_f = \pi/2$ and $3\pi/2$ tend to have a high constraint value in collision avoidance. This is because these angles correspond to the position that is on the semi-minor axis of the osculating invariant circle at apolune, which is closer to the KOZ (cf. Fig. 9).

Analysis on Passively Safe Reconfiguration

The analysis in the previous subsection suggests that careful choice of the departure and arrival phases is important for the relative trajectory design between the QPROs around the NRHO. Since it takes approximately 8 orbits for the relative orbits to return to a similar torus state in $\mathbb{T}^2$ (cf. Figure 7), a transfer might be considered between particular phases of QPROs, for which a plain OCP solution lacks passive safety. This subsection evaluates the two passive safety strategies proposed by comparing their fuel efficiency and the geometric characteristics of the resulting trajectories. In this case study, a representative pair of phases is chosen as $(\theta_i, \theta_f) = (4.2, 0)$.

This paper adopts `SCvx⋆`[37] as an SCP algorithm. The solution to the nonconvex problem incorporating the drift-safe constraint in Eq. (27) is referred to as SCP-DRIFT, while the solution to the nonconvex problem using the first-order QPRIT criterion in Eq. (29) is termed SCP-QPRIT. For the SCP-DRIFT, the solution of the plain OCP serves as the initial guess. The one-orbit drift safety is enforced in the form of Eq. (27), where the drifting time is discretized by $N_{\text{safe}} = 30$. In contrast, for the SCP-QPRIT, the convex solution of the plain OCP with the l_2-norm constraint (cf. Eq. (29a)) serves as the initial guess. For the constraints in Eq. (29a), the parameters are chosen as $\epsilon_h = 0.1$m, $\epsilon_{\dot{h}} = \epsilon_{\dot{\alpha}} = \epsilon_{\dot{\beta}} = 3$ mm/s.

Both problems converged to the local optimum, and the optimized trajectories are illustrated in Figures 11 and 12, respectively. Trajectories are resolved in both the TNW frame and the LVLH frame, and the

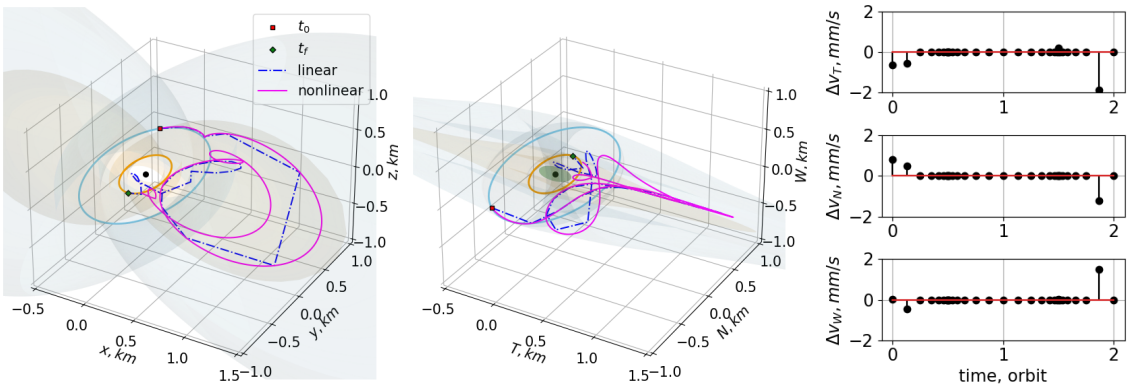

(a) LVLH frame (b) TNW frame (c) Control History (TNW frame)

Figure 11: Optimized Trajectory of the SCP-DRIFT in the local frames.

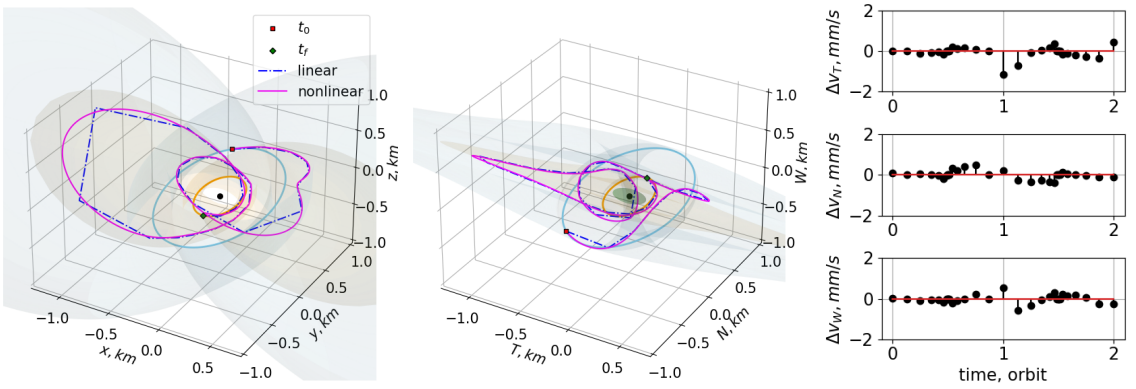

(a) LVLH frame (b) TNW frame (c) Control History (TNW frame)

Figure 12: Optimized Trajectory of the SCP-QPRIT in the local frames.

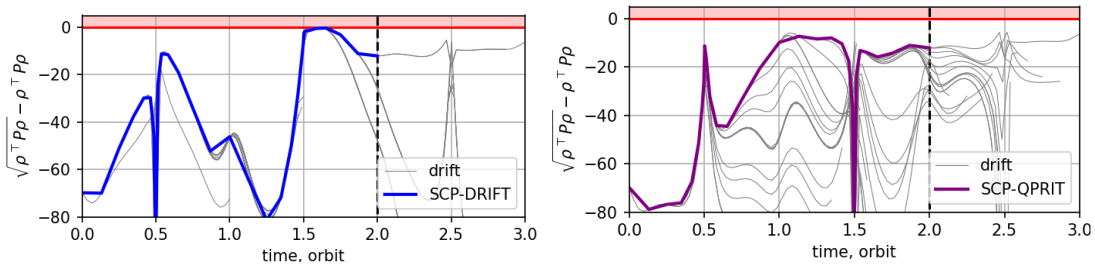

(a) SCP-DRIFT (b) SCP-QPRIT

Figure 13: Satisfaction of the passive safety constraint for drift trajectories.

impulsive control profile is also shown in each figure. The light blue and orange surfaces are the (first-order) initial and terminal QPRIT, respectively. Bold ellipses attached to the QPRITs illustrate the invariant circle at the initial and terminal epoch. Furthermore, the control profile is propagated along the nonlinear relative dynamics of the CR3BP, and the resulting nonlinear trajectories (solid magenta) are compared to

the optimized linear trajectories (dotted blue). Additionally, the passive safety constraint in Eq. (27a) is evaluated for each optimized trajectory and summarized in Figure 13. The state below the red line indicates the satisfaction of the safety constraint. It is confirmed from these figures that the one-orbit passive safety is achieved in both optimal trajectories. The SCP-DRIFT converges to a total Δv_{tot} of $4.805 \cdot 10^{-3}$ m/s, whereas the SCP-QPRIT yields a total Δv_{tot} of $8.369 \cdot 10^{-3}$ m/s. The transfer cost is higher in the SCP-QPRIT due to the conservative nature of the passive safety constraint. It is evident from Figure 11b that the controlled trajectory is inside the surface of the QPRIT that corresponds to the terminal state and makes a tangent contact with the surface of the KOZ. On the other hand, the converged solution of SCP-QPRIT ensures that the deputy not only remains outside of the terminal QPRIT but also leverages the dynamical structure by staying on the surface of QPRIT throughout the transfer. Thus, the worst (maximum) constraint value shown in Figure 13b is far below the constraint violation threshold. A comparison of Figures 11c and 12c highlights the distinct optimal control strategies. While the SCP-DRIFT yields a control history resembling a two-impulse solution, the SCP-QPRIT solution spreads small impulses across the transfer, ensuring adherence to the QPRIT surface at each time step and the smooth transition along the QPRIT surface from the initial to the terminal state. Notably, this strategy helps mitigate the nonlinear error between the optimized linear trajectory and the propagated nonlinear trajectory, as shown in Figure 12c. The suppression of the nonlinear error is naturally considered in the LTC-based constraint, posing another advantage for passively safe cislunar relative motion control. In contrast, a significant nonlinear gap develops after the first orbit in the SCP-DRIFT due to large initial impulses, as shown in Figure 11.

Figure 14 re-plots the optimal trajectories are re-plotted in the LTC. In addition to the two optimal solutions, the solution of the plain OCP is also presented. The solutions of the plain OCP and SCP-DRIFT exhibit significant variations in the h component, which is orthogonal to the local eigenspace. This indicates a separation from the QPRIT surface and a loss of quasi-periodicity during the transfer. Furthermore, although these solutions include a segment with a radius (ε) smaller than the terminal radius (ε_f), the SCP-DRIFT solution retains one-orbit passive safety. This is because a passive safety constraint given by Eq. (27a) does not evaluate infinite-time passive safety under natural dynamics. Conversely, the SCP-QPRIT solution remains constrained within the eigenspace and avoids entering the terminal radius, ensuring passive safety through the evaluation of the LTC. This is an advantage of using the LTC in the OCP, where the safety condition is geometrically evident. While most plain OCP solutions exhibit one-orbit passive safety, as illustrated in Figure 10c, incorporating safety constraints in the LTC leads to a trajectory design that is more practical for operational use.

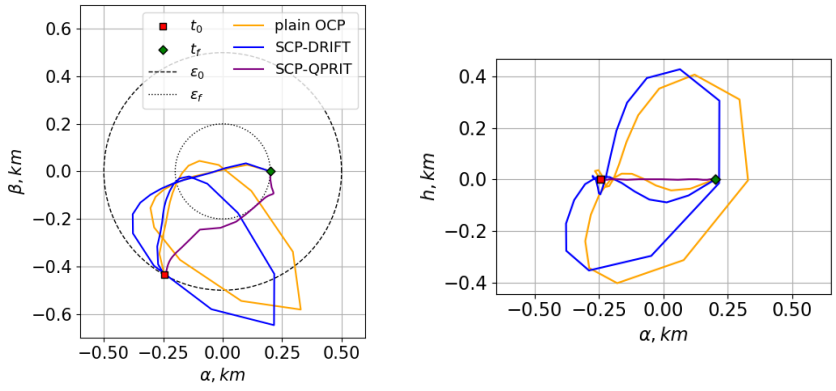

(a) $\alpha - \beta$ plane (b) $\alpha - h$ plane

Figure 14: Optimal trajectories in the nonsingular local toroidal coordinates.

Validation with a High-Fidelity Dynamics Model

As the optimal control profile obtained is based on a linear relative CR3BP model, this subsection provides the validation of the generated trajectories in a high-fidelity dynamics model. This considers the full-ephemeris point-mass model of the Sun-Earth-Moon system with solar radiation pressure (SRP). For the positions of the celestial bodies, the ephemeris data is based on the SPICE kernel*. The acceleration due to SRP is modeled as follows:[27]

$$[\ddot{\boldsymbol{r}}_{\text{SRP}}]_{\mathcal{I}} = -\frac{p_{\text{SRP}} c_r A_{\text{SRP}}}{m} \frac{\boldsymbol{r}_s}{r_s}, \tag{31}$$

where $\boldsymbol{r}_s$ denotes the position vector from the Sun to the spacecraft. The solar radiation pressure is set as $p_{\text{SRP}} = 4.57 \cdot 10^{-6}$ N/m^2, the reflectivity is set as $c_r = 1.0$, the averaged exposed cross-sectional area to the Sun is set as $A_{\text{SRP}} = 1$ m^2, and the mass of the spacecraft is set as $m = 100$ kg. In this paper, the cannonball model is used, where the shape of the spacecraft is approximated as a sphere. The deputy's state was propagated using the high-fidelity model with its initial state and control history. The initial state of the chief was taken from the apolune condition of the periodic CR3BP solution of the NRHO, and no additional station-keeping control was considered. The motions of the two spacecraft were propagated in the inertial frame with the LSODA integrator[38] and then converted to a local frame.

Figures 15a and 15b show the positional error of the linear relative dynamics to the high-fidelity dynamics along the transfer, for the obtained optimal control profiles from both SCP solutions. They also display the results of an ablation study that was conducted to assess the sensitivity of the error to each force included in the high-fidelity dynamics model. There is a clear divergence between the high-fidelity and CR3BP models, although the motion remains bounded for the duration of the transfer. The history of the positional error indicates that the largest errors occur at perilune, based on the sharp increases in errors halfway through each orbit. This is expected as spacecraft move faster at perilune, making the relative motion more sensitive to the nonlinear gap in the dynamics modeling. Furthermore, the similarities in the error history across all variations of the high-fidelity ground truth in Figures 15a and 15b suggest that the position error of the linear dynamics is almost entirely due to the forces included in the simplest version of the high-fidelity model – full-ephemeris Earth and Moon gravity – not solar gravity or SRP. This implies a limitation of the CR3BP model in the Earth-Moon system, as the Moon's eccentricity must be addressed to make an easier transition from the low-fidelity dynamics models to the high-fidelity model.

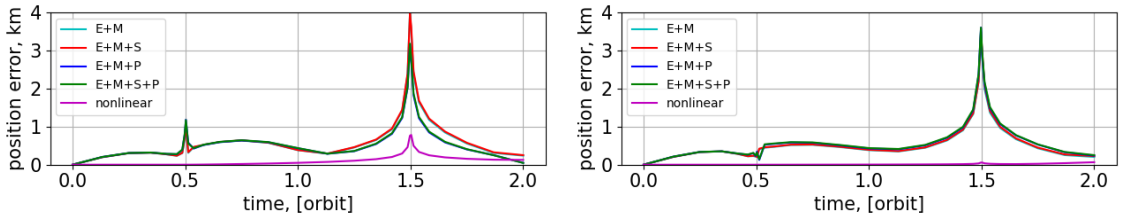

(a) SCP-DRIFT

(b) SCP-QPRIT

Figure 15: Position error of linear relative CR3BP dynamics compared to nonlinear relative CR3BP dynamics and high-fidelity dynamics models. E = Earth Gravity, M = Moon Gravity, S = Solar Gravity, P = Solar Radiation Pressure. Orbits start at apolune.

CONCLUSION

With the anticipated rise in cislunar operations, safety of bounded relative motion in cislunar orbits becomes essential. This paper presents passively safe relative motion control strategies in the Circular-Restricted Three-Body Problem (CR3BP). First, the relative motion in the CR3BP is resolved in a co-moving frame

*https://naif.jpl.nasa.gov/naif/toolkit.html

whose first axis is aligned to the chief spacecraft's velocity direction. Furthermore, the structure of the first-order two-dimensional quasi-periodic invariant torus is analyzed in the local eigenspace that corresponds to the oscillatory mode. The geometric relationship of these eigenvectors and the relative eccentricity and inclination vectors in relative motions in the restricted two-body problems is rendered. Finally, a passively safe optimal reconfiguration between two quasi-periodic orbits is formulated as an optimal control problem in the local toroidal coordinates. While two nonconvex passive safety strategies are explored, the constraints in the local toroidal frame particularly offer geometric insights into passive safety through the dynamical structure of the quasi-periodic relative invariant tori. This provides a general but simple safety measure for relative motion control on any periodic orbits in the CR3BP that contain an oscillatory mode. Future research includes the addition of station-keeping and tracking schemes with uncertainties, as well as the extension of this work in the elliptic-restricted three-body problem to close the dynamics modeling gap illustrated by the high-fidelity validation.

ACKNOWLEDGMENTS

This work is supported by Blue Origin (SPO #299266) as an Associate Member and Co-Founder of the Stanford's Center of AEroSpace Autonomy Research (CAESAR), and National Science Foundation Graduate Research Fellowship Program (No. DGE-2146755). This article solely reflects the opinions and conclusions of its authors and not any sponsors. Yuji Takubo acknowledges financial support from the Ezoe Memorial Recruit Foundation. The authors thank Ethan Foss and Pauline de la Hogue Moran for insightful discussions.

REFERENCES

[1] W. H. Clohessy and R. S. Wiltshire, "Terminal Guidance System for Satellite Rendezvous," *Journal of the Aerospace Sciences*, Vol. 27, Sept. 1960, pp. 653–658, 10.2514/8.8704.

[2] K. Yamanaka and F. Ankersen, "New State Transition Matrix for Relative Motion on an Arbitrary Elliptical Orbit," *Journal of Guidance, Control, and Dynamics*, Vol. 25, Jan. 2002, pp. 60–66, 10.2514/2.4875.

[3] S. D'Amico, *Autonomous formation flying in low earth orbit*. PhD thesis, TU Delft, 2010.

[4] J. Sullivan, S. Grimberg, and S. D'Amico, "Comprehensive survey and assessment of spacecraft relative motion dynamics models," *Journal of Guidance, Control, and Dynamics*, Vol. 40, No. 8, 2017, pp. 1837–1859.

[5] A. W. Koenig, T. Guffanti, and S. D'Amico, "New state transition matrices for spacecraft relative motion in perturbed orbits," *Journal of Guidance, Control, and Dynamics*, Vol. 40, No. 7, 2017, pp. 1749–1768.

[6] S. D'Amico, J.-S. Ardaens, and R. Larsson, "Spaceborne autonomous formation-flying experiment on the PRISMA mission," *Journal of Guidance, Control, and Dynamics*, Vol. 35, No. 3, 2012, pp. 834–850.

[7] J. S. Ardaens and S. D'Amico, "Control of Formation Flying Spacecraft at a Lagrange Point," *Technical Note*, 2008.

[8] J. Kruger, A. W. Koenig, and S. D'Amico, "Starling formation-flying optical experiment (starfox): System design and preflight verification," *Journal of Spacecraft and Rockets*, Vol. 60, No. 6, 2023, pp. 1755–1777.

[9] S. Lowe, D. Fitzpatrick, A. Buynovskiy, L. Shoemaker, S. Palo, and S. D'Amico, "Concept of Operations for SWARM-EX: a Three CubeSat Formation-Flying Mission," *2024 IEEE Aerospace Conference*, IEEE, 2024, pp. 1–13.

[10] T. Guffanti, T. Bell, S. Y. Low, M. Murray-Cooper, and S. D'Amico, "Autonomous Guidance Navigation and Control of the VISORS Formation-Flying Mission," *2023 AAS/AIAA Astrodynamics Specialist Conference, Big Sky, MT.*, 2023.

[11] D. J. Scheeres, F.-Y. Hsiao, and N. X. Vinh, "Stabilizing motion relative to an unstable orbit: applications to spacecraft formation flight," *Journal of Guidance, Control, and Dynamics*, Vol. 26, No. 1, 2003, pp. 62–73.

[12] A. M. Segerman, M. F. Zedd, and F. H. Bauer, "Preliminary planar formation-flight dynamics near sun-earth l2 point," *2003 AAS/AIAA Space Flight Mechanics Meeting*, No. AAS-03-133, 2002.

[13] G. Franzini and M. Innocenti, "Relative Motion Dynamics in the Restricted Three-Body Problem," *Journal of Spacecraft and Rockets*, Vol. 56, Sept. 2019, pp. 1322–1337, 10.2514/1.A34390.

[14] F. Khoury and C. Lippe, "Relative Guidance, Navigation, and Control, in Multibody Gravitational Regimes," *AAS/AIAA Astrodynamics Specialist Conference*, Charlotte, NC, 2022.

[15] J. O. Romero and F. Khoury, "Cislunar Proximity Operations in the Bicircular Restricted Four Body Problem," *2023 Advanced Maui Optical and Space Surveillance Technologies (AMOS) Conference, Maui, HI*, 2023.

[16] B. Marchand and K. Howell, "Control strategies for formation flight in the vicinity of the libration points," *Journal of guidance, control, and dynamics*, Vol. 28, No. 6, 2005, pp. 1210–1219.

[17] M. Bando and A. Ichikawa, "Formation flying along halo orbit of circular-restricted three-body problem," *Journal of Guidance, Control, and Dynamics*, Vol. 38, No. 1, 2015, pp. 123–129.

[18] B. T. Barden, "Formation flying in the vicinity of libration point orbits Spaceflight mechanics 1998," *Proceedings of the AAS/AIAA Space Flight Mechanics Meeting, Monterey, 1998*, 1998, pp. 969–988.

[19] I. L. Elliott, *Relative Trajectory Design and Control near Periodic Orbits in Multi-Body Systems using Local Toroidal Coordinates*. PhD thesis, University of Colorado at Boulder, 2022.

[20] F. Khoury, R. Power, P. Ghosh, and J. O. Romero, "Relative-Navigation-Informed Formation Configuration and Station-Keeping Strategies in the Earth-Moon-Sun System," *2024 AAS/AIAA Astrodynamics Specialist Conference*, Broomfield, CO, 2024.

[21] H. Sekine, Y. Kawabata, K. Oguri, and R. Funase, "Guidance and Control of Formation Flying Reconfiguration Considering Collision Avoidance in the CRTBP.," *2024 AAS/AIAA Astrodynamics Specialist Conference, Bloomfield, CO*, 2024.

[22] I. Elliott and N. Bosanac, "Describing relative motion near periodic orbits via local toroidal coordinates," *Celestial Mechanics and Dynamical Astronomy*, Vol. 134, No. 2, 2022, p. 19.

[23] T. Guffanti and S. D'Amico, "Passively Safe and Robust Multi-Agent Optimal Control with Application to Distributed Space Systems," *Journal of Guidance, Control, and Dynamics*, Vol. 46, No. 8, 2023, pp. 1448–1469.

[24] D. A. Marsillach, S. Di Cairano, and A. Weiss, "Fail-safe rendezvous control on elliptic orbits using reachable sets," *2020 American Control Conference (ACC)*, IEEE, 2020, pp. 4920–4925.

[25] S. D'Amico and O. Montenbruck, "Proximity operations of formation-flying spacecraft using an eccentricity/inclination vector separation," *Journal of Guidance, Control, and Dynamics*, Vol. 29, No. 3, 2006, pp. 554–563.

[26] Y. Takubo, T. Guffanti, M. Gammelli D., Pavone, and S. D'Amico, "Towards Robust Spacecraft Trajectory Optimization via Transformers," *2025 IEEE Aerospace Conference, Big Sky, MT (Accepted)*, 2025.

[27] D. Vallado, *Fundamentals of Astrodynamics and Applications, Fifth Edition*. Space Technology Library, 2022.

[28] A. W. Koenig and S. D'Amico, "Robust and safe N-spacecraft swarming in perturbed near-circular orbits," *Journal of Guidance, Control, and Dynamics*, Vol. 41, No. 8, 2018, pp. 1643–1662.

[29] Z. P. Olikara, *Computation of quasi-periodic tori and heteroclinic connections in astrodynamics using collocation techniques*. PhD thesis, University of Colorado at Boulder, 2016.

[30] N. Baresi, *Spacecraft formation flight on quasi-periodic invariant tori*. PhD thesis, University of Colorado at Boulder, 2017.

[31] D. E. Lee, "Gateway destination orbit model: A continuous 15 year NRHO reference trajectory," *NASA Johnson Space Center White Paper*, 2019.

[32] R. Nakamura, J. Kikuchi, T. Sasaki, Y. Matsumoto, M. Hidaka, N. Murakami, S. Ueda, and N. Satoh, "Rendezvous trajectory design of logistics resupply missions to the lunar gateway in near-rectilinear halo orbit," *Journal of Space Safety Engineering*, Vol. 10, No. 2, 2023, pp. 144–154.

[33] T. Guffanti, *Optimal passively-safe control of multi-agent motion with application to distributed space systems*. PhD thesis, Stanford University, 2022.

[34] J. Leith and R. P. Russell, "A time regularization scheme for spacecraft trajectories subject to multi-body gravity," *The Journal of the Astronautical Sciences*, Vol. 70, No. 2, 2023, p. 7.

[35] K. F. Sundman, "Mémoire sur le problème des trois corps," *Acta mathematica*, Vol. 36, No. 1, 1913, pp. 105–179.

[36] D. Morgan, S.-J. Chung, and F. Y. Hadaegh, "Model predictive control of swarms of spacecraft using sequential convex programming," *Journal of Guidance, Control, and Dynamics*, Vol. 37, No. 6, 2014, pp. 1725–1740.

[37] K. Oguri, "Successive convexification with feasibility guarantee via augmented lagrangian for non-convex optimal control problems," *2023 62nd IEEE Conference on Decision and Control (CDC)*, IEEE, 2023, pp. 3296–3302.

[38] L. Petzold, "Automatic selection of methods for solving stiff and nonstiff systems of ordinary differential equations," *SIAM journal on scientific and statistical computing*, Vol. 4, No. 1, 1983, pp. 136–148.